metals

MDPI

Article

Comprehensive Characterisation of a Newly Developed Mg–Dy–Al–Zn–Zr Alloy Structure

Lenka Kunčická * and Radim Kocich

Regional Materials Technology and Science Centre (RMTSC), Faculty of Metallurgy and Materials Engineering, VŠB—Technical University of Ostrava, 17. listopadu 15, Ostrava 708 00, Czech Republic; radim.kocich@vsb.cz
* Correspondence: lenka.kuncicka@vsb.cz; Tel.: +420-597-324-433

Received: 16 December 2017; Accepted: 16 January 2018; Published: 19 January 2018

Abstract: This is a report on the structure phases and precipitates in a newly developed Mg–10Dy–3Al–1Zn–0.2Zr alloy. Specimens from the cast alloy were heat treated at temperatures of 480 °C, 520 °C and 560 °C, all for 8 and 16 h, and subsequently quenched. The structures were then analysed using scanning and transmission electron microscopy, while the mechanical properties were investigated using microhardness measurements. The results showed the different temperatures, as well as times, influence both the chemical composition and morphology of the precipitated phases. The occurrence of the β-phase changed with increasing temperature and time from grain boundary segregations through fine elongated particles to coarse plate-like precipitates. Polygon-shaped Dy-rich precipitates were observed in all the samples; however, their size decreased and their distribution homogenised with increasing annealing temperature and time. The samples annealed at 520 °C and 560 °C exhibited the presence of lamellar 18R-type long period stacking ordered (LPSO) phases. Microhardness measurements were in accordance with results of the microscopic analyses; although the values varied between 60 and 65 HV for all the material states, the most uniform distribution was observed for the 560 °C/8-h sample, which featured the finest precipitates and LPSO phases.

Keywords: magnesium; precipitates; β-phase; SEM; TEM

1. Introduction

Automotive [1] and aerospace [2], as well as biomechanics [3,4], are just a few examples of the main research and industry branches aimed at advanced lightweight materials, the everlasting research and development of which has resulted in the design of new innovative Mg-based alloys and their production technologies [5]. The mechanical and physical properties are not the greatest advantages of pure Mg; however, they can both be improved by structural unit refinement and the addition of alloying elements [6].

Refinement of the structural units can be provided via plastic deformation [7] (advantageously via severe plastic deformation (SPD) methods [8] such as equal channel angular pressing [9,10], high pressure torsion [11], and accumulative roll bonding [12]), processing via methods of powder metallurgy (PM) [13], by combinations of PM and SPD [14], or via additions of structure refining elements. Since Mg-based alloys in industry are usually used for die-casting [15], the effects of the alloying elements are of the utmost importance.

The alloying elements can positively affect the mechanical properties of Mg-based alloys in many ways: for example, by grain refinement, solid solution strengthening, and precipitation hardening [16,17]. Aluminium, a common alloying element, provides strengthening via solid solution and precipitation of secondary phases, especially $Mg_{17}Al_{12}$ [18,19]. Additions of zinc lead to the formation of Mg–Zn Guinier–Preston zones and precipitation of $MgZn_x$ strengthening phases;

in Mg–Al-based alloys, zinc also contributes to the refinement of the $Mg_{17}Al_{12}$ phase [18]. Alloying by rare earth (RE) metals generally induces precipitation and grain refinement [20]. Additions of RE can also increase plasticity and thus ensure better formability even during severe plastic deformation treatment at room temperature. For example, additions of La or Y result in the strengthening of Mg-based alloys to more than 400 MPa after processing via extrusion at elevated temperatures [21,22]. The strength of Mg–RE alloys can advantageously be further increased by the addition of Zn, which contributes to the formation of various Mg–RE–Zn long-period stacking ordered (LPSO) phases. These have been reported to feature favourable mechanical properties [23]. Therefore, Mg–RE–Zn alloys are very good candidates for lightweight construction applications. However, similar to grains and precipitates, large and coarse LPSO phases do not contribute to improvements in the mechanical properties as much as fine phases do [24]. Zirconium has a strong refining effect [18] and its addition to Mg-based alloys containing RE usually result in quite notable improvements in the mechanical properties [25]. The effect of Zr on grain refinement is the most favourable when its content is below 17 wt. % [26]. Conjunctive additions of RE, Zn and Zr also result in the formation of (meta)stable precipitates and RE-rich phases after heat treatments [27,28]. Precipitation is quite an issue for Mg-based alloys since this phenomenon can significantly influence mechanical as well as physical properties. Precipitation can be controlled by various means, such as the chemical composition [29], imposed strain [30,31], and the selected heat treatment regime [32].

This work deals with the investigation of a recently designed Mg–10Dy–3Al–1Zn–0.2Zr alloy. The alloy is based on the AZ31 alloy featuring improved mechanical properties and corrosion resistance when compared to pure Mg [18]. The AZ alloys are among the most advantageous alternatives to steel in many structural and industrial applications [33,34], but they can also be used in biomedicine [35]. Dy has a favourable effect on strengthening and structure stabilisation, similar to other RE metals, and is also considered to be biocompatible [29,36]. Additions of Dy to Mg-based alloys significantly improve corrosion resistance in various solutions [18]. The amount of added Dy was selected based on the literature research—Mg-10Dy alloys are reported to have very favourable mechanical properties [37], as well as corrosion resistance [36] (higher amounts of Dy significantly decrease plasticity as well as increase the corrosion rate). As already mentioned, Zr has a strong refining effect and also exhibits excellent biocompatibility [38]. Therefore, despite the fact that the alloy was designed to be applicable for construction purposes, it can also be considered for biomedical purposes due to the favourable chemical composition [36,39,40].

Whereas our previous study was focused on the influence of SPD processing on the structure of the alloy [41], the herein presented study was designed with the aim to compare the effects of different heat treatments on the precipitated phases, their sizes and morphologies. The fact that ageing treatments conducted at temperatures between 200 °C and 350 °C support development of the strengthening phases in Mg-based alloys is known and has been reported by others (e.g., [42,43]). However, too high temperatures and times can lead to over-ageing and coarsening of the precipitates. For example, Apps et al. [44] reported the effect of increasing the ageing time period on coarsening of Mg–RE precipitates, and Rokhlin [20] reported decreasing mechanical properties of Mg–Dy-based alloys to be related to the effect of increasing ageing temperature. This study is a report on the structure and substructure of the alloy subjected to different heat treatments; the selected temperatures were higher and the times were shorter than for conventional ageing treatments and the effects are discussed with conclusions drawn from the available literature. The first annealing temperature applied was 520 °C. This temperature is most commonly used for solution treatments of Mg-based alloys with additions of RE metals according to the available literature [13,26,28–32]. At 520 °C, the two time periods of 8 and 16 h were applied, and also for two different temperatures of 480 °C and 560 °C. The temperature of 480 °C was selected as the lower temperature limit since no significant structure rearrangement has been found in Mg–RE-based alloys when annealed below 480 °C for relatively short times [45]; the value of 560 °C was selected based on the maximum solubility of Dy in Mg being at 561 °C [20]. The 8-h treatment was selected based on the research of Mg–Dy-based alloys performed by others (e.g., Mg–Dy–Gd–Zr [39], Mg–Dy–Zn [46,47], etc.); the time of 16 h (double the first time period) was selected to observe possible structural changes after exposure to the identical temperature for a longer time. The sizes of the precipitated phases and their effects on the mechanical properties were also evaluated. However, deeper studies addressing the precipitation kinetics and diffusion parameters are planned for a subsequent publication.

2. Materials and Methods

The AZ31 alloy with the original composition determined by optical spectroscopy analyses being Mg + 2.7 wt. % Al + 0.7 wt. % Zn was melted with additions of slivers of Dy (10 wt. %) and Zr (0.2 wt. %) and cast using a Supercast vacuum induction furnace. After casting, the alloy was cooled naturally in a little rod with the length of 50 mm and diameter of 20 mm. From the rod, 3 mm thick discs were cut for the subsequent investigations. According to the optical spectroscopy, the overall composition of the as-cast alloy was 90.4 wt. % Mg + 7.3 wt. % Al + 0.6 wt. % Zn + 1.6 wt. Dy + 0.1 wt. % Zn. Throughout the text, the measured average element content values were rounded to one decimal due to the measurement of five different locations and counting with possible inaccuracy of the energy dispersive spectroscopy (EDX, Tescan s.r.o., Brno, Czech Republic) method, especially for very low contents. However, the compositions of the individual investigated secondary phases were rounded to two decimals, primarily due to the very little Zr overall content.

After cutting the disc samples, the annealing temperatures of 480 °C, 520 °C and 560 °C were applied, all for 8 and 16 h. After annealing, the samples were quenched immediately in chilled water with an average cooling speed of approximately 10 °C/s. The basic temperature for this alloy was selected as 520 °C; the results of this treatment had been presupposed to provide a comparative reference for the other samples heat treated at the different temperatures.

Samples for scanning electron microscopy (SEM, Tescan s.r.o., Brno, Czech Republic) investigations were polished using Struers OPS silica solution (Struers GmbH, Berlin, Germany) and subsequently electropolished. The chemical compositions of the material and the individual phases and the microstructures were investigated using a Tescan Lyra 3 FIB/SEM device (Tescan s.r.o., Brno, Czech Republic) equipped with a NordlysNano EBSD detector (Oxford Instruments, Abingdon, UK). The samples for transmission electron microscope (TEM) observations were prepared by a twin-jet electropolishing device (Tescan s.r.o., Brno, Czech Republic) and analysed using a JEOL 2100F TEM equipment (JEOL Ltd., Tokyo, Japan) operating at 200 kV. Image analyses of the particles' sizes and volumes were performed using the ImageJ software. HV0.2 Vickers microhardness (FM ARS 900 device, Futuretech corp., Kawasaki, Japan) was measured with a diamond indenter in two perpendicular directions across the samples' diameters; the spacing of the individual locations was 1 mm starting 0.5 mm from the edge.

3. Results

3.1. Microstructures

3.1.1. As-Cast State

The optical micrograph and SEM-BSE (scanning electron microscope—back-scattered electrons diffraction) image of the as-cast material are depicted in Figure 1. The first analyses were focused on determining the contents of the individual elements. For these observations, five locations picked randomly from the cast material (to reduce inaccuracies introduced by possible segregations and inhomogeneities) were subjected to EDX chemical composition analyses. According to the results, the average overall chemical composition of the as-cast alloy, as depicted in Table 1, was rather homogeneous throughout the rod. However, the material consisted of three main phases: the solid solution (SS) containing the major portion of Mg, the Mg-rich segregated phases, and the Dy-rich precipitates (observed in Figure 1b as the black matrix, segregations in shades of grey, and white particles, respectively). The average chemical compositions of all the present phases (in wt. %) can be found in Table 1. A very small amount of zirconium was added to provide the material with precipitation strengthening and strengthening via grain refinement. In accordance with these presumptions, Zr was found primarily in the Dy-rich precipitates.

For the as-cast material, the grain size was also determined by measuring the maximum ferret diameters of the individual grains. The results of the analyses showed that almost 50% of the grains had diameters smaller than 10 μm, while the average grain size was 16.5 μm (not shown here).

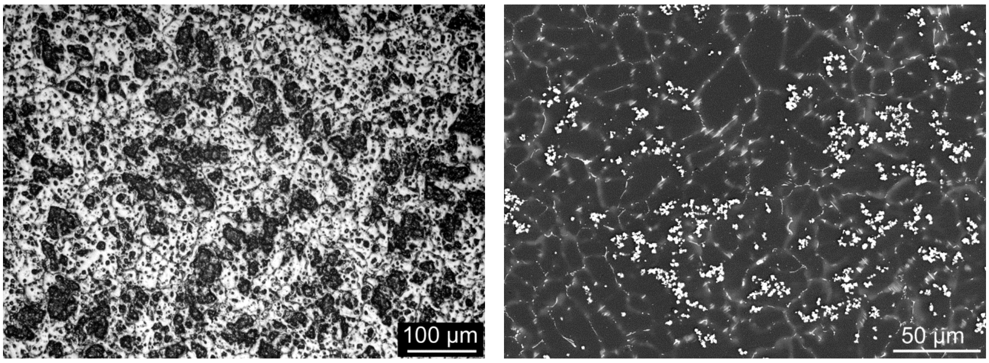

(**a**) (**b**)

Figure 1. As-cast state: (**a**) optical micrograph; (**b**) scanning electron microscopy image.

Table 1. Average chemical composition of the phases within the as-cast alloy.

Element (wt. %)	Mg	Al	Zn	Dy	Zr
Mg matrix	94.8	4.5	0.3	0.3	0.1
Segregations	71.4	24.8	2.6	1.1	0.1
Precipitates	40.7	25.3	1.2	32.5	0.3

3.1.2. Heat Treatment at 520 °C

An SEM-BSE image of the alloy heat treated at 520 °C for 8 h is depicted in Figure 2. Although the two selected time periods at this given annealing temperature did not impart evident differences in the appearance of the observed phases or their chemical compositions, the sample that was annealed for 8 h exhibited a greater occurrence of both phases—segregated β-phase and polygon-shaped precipitates—than the sample annealed for 16 h (not shown here). The longer annealing treatment imparted more efficient dissolution of the secondary phases into the SS. By this reason, the matrix in the 16-h sample exhibited a higher presence of the alloying elements (the average matrix chemical compositions were 92.5 wt. % Mg, 3.5 wt. % Al, 0.6 wt. % Zn, 3.3 wt. % Dy plus 0.1 wt. % Zr for the 8-h sample and 90.8 wt. % Mg, 4.4 wt. % Al, 0.9 wt. % Zn, 3.7 wt. % Dy plus 0.2 wt. % Zr for the 16-h sample).

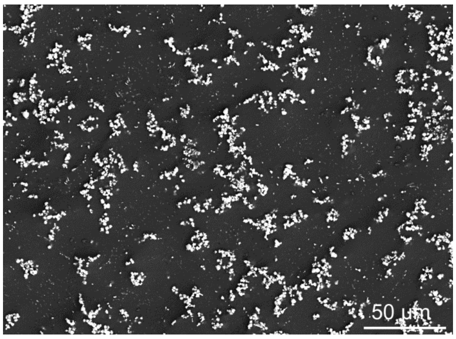

Figure 2. SEM-BSE (scanning electron microscope—back-scattered electrons diffraction) scan of the heat treated sample (520 °C/8 h).

The distribution maps of the individual elements acquired using SEM-EDX chemical composition mapping within a selected area of the 520 °C/8-h sample are shown in Figure 3. The analysis showed the major portion of Mg to be present in the matrix, whereas the other elements were primarily present in the secondary phases. The overall content of Zr was very low. Therefore, the mapping was not able to accurately determine its distribution.

Al was present in all the three phases, including the matrix in which it dissolved into the SS and thus provided the material with solid solution strengthening. Dy was present especially in the polygon-shaped precipitates; however, the segregated phase also contained small amounts of Dy. Zn was primarily observed in the segregated phases, which can thus be characterised as the $Mg_{17}(AlZnDy)_{12}$ β-phase. The fine precipitates were further observed in more detail via TEM.

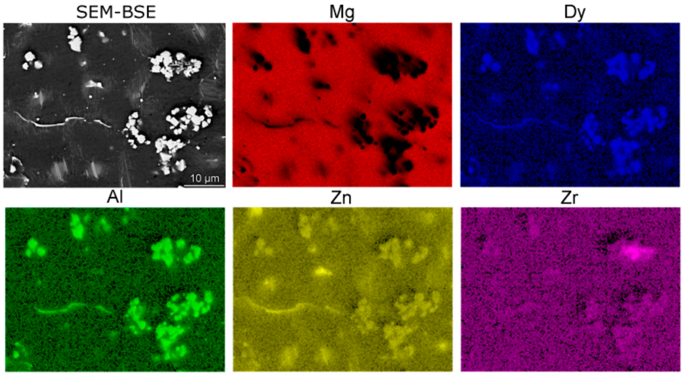

Figure 3. Distribution of the individual elements within the selected area of the 520 °C/8-h sample.

The structures of both the 8-h and 16-h samples contained large precipitates (with sizes exceeding 1 µm) featuring very high amounts of Dy (more than 90 wt. %). However, they were observed especially in the 520 °C/8-h sample due to better Dy dissolution when annealed for 16 h. One such precipitate together with the corresponding SAED (Selected area electron diffraction) pattern is depicted in Figure 4a. The comparison of the experimental and ideal diffraction patterns showed the precipitate to consist primarily of cubic Dy (unit cell *a*, *b*, *c* = 5.18 A and α, β, γ = 90°). The chemical composition measurement confirmed the major element in the particle to be Dy (about 97 wt. %).

A TEM micrograph showing a detailed view of the precipitates in the 520 °C/16-h sample is depicted in Figure 4b, which reveals several different morphologies of the precipitates. The structure contained precipitates with sharp edges (polygon-shaped) with very high amounts of Dy (e.g., locations 1 and 2), as well as elongated thin precipitates (location 3) containing Mg, Dy and Zn. The compositions of the individual precipitates are depicted in Table 2.

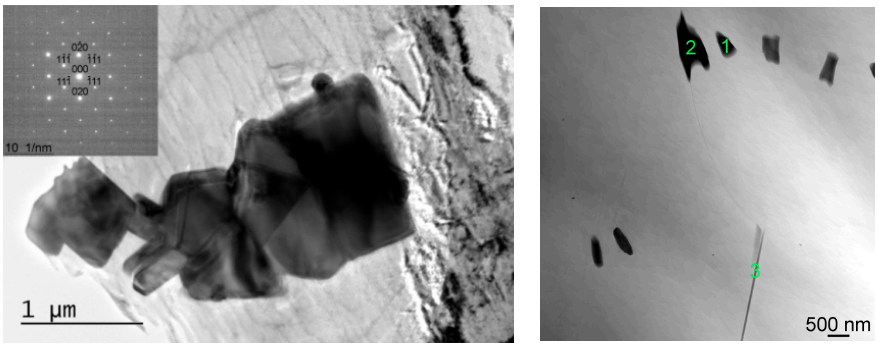

(**a**) (**b**)

Figure 4. (**a**) TEM (transmission electron microscope)image of the 520 °C/8-h sample with precipitate SAED (Selected area electron diffraction) pattern; (**b**) TEM image of the 520 °C/16-h sample.

Table 2. Chemical compositions of the precipitates in locations 1–3 in Figure 4b (520 °C/16-h sample).

Element (wt. %)	Mg	Al	Zn	Dy	Zr
1	27.22	3.28	0.34	69.08	0.08
2	19.75	5.19	3.82	71.18	0.06
3	77.46	0.04	3.31	19.17	0.02

3.1.3. Heat Treatment at 480 °C

The annealed structure of the 480 °C/8-h sample is depicted in Figure 5. Especially the sample heat treated for 8 h still exhibited segregation of the continuous β-phase at the grain boundaries; however, they were much less evident than in the as-cast state (Figure 1b). The distribution of the precipitates was also less homogeneous than in the 520 °C samples and the amount of the dissolved Dy in the SS was lower (approximately 2.8 wt. % for both the samples). In addition, the longer annealing time imparted a tendency for particle clustering (i.e., the inter-particle distance was smaller).

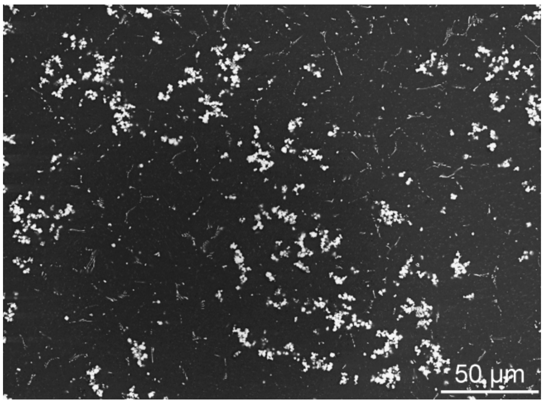

Figure 5. SEM-BSE scan of the 480 °C/8-h heat treated sample.

Figure 6 taken from the 480 °C/8-h sample showing the polygon-shaped precipitates forming clusters imparts insufficient Dy dissolution and an aggravated diffusion process at this temperature. This was also confirmed by measurements of the chemical compositions of the precipitates (Spectrum 1–4 in Figure 6), which showed the average composition of the precipitates to be 6.2 wt. % Mg, 8.1 wt. % Al, 0.2 wt. % Zn, 85.2 wt. % Dy plus 0.3 wt. % Zr. The fact that Zr was only detected in the very small precipitate depicted as Spectrum 4 should be stressed.

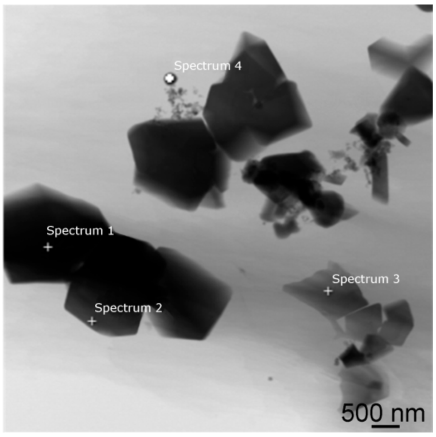

Figure 6. TEM image of the 480 °C/8-h sample.

The distribution maps for the individual elements within the 480 °C/8-h sample are depicted in Figure 7a. The results showed the grain boundary segregations to contain especially Zn and a small portion of Dy, while Al was primarily present in the polygon-shaped Dy-rich precipitates. The composition of several precipitates was determined via EDX and the results are depicted in Table 3. Locations 1, 2 and 3 represent the polygon-shaped Dy-rich precipitates, while fine lamellar particles depicted at locations 4, 5 and 6 correspond to the grain boundary segregated β-phase. The analysed secondary phases are depicted in Figure 7b.

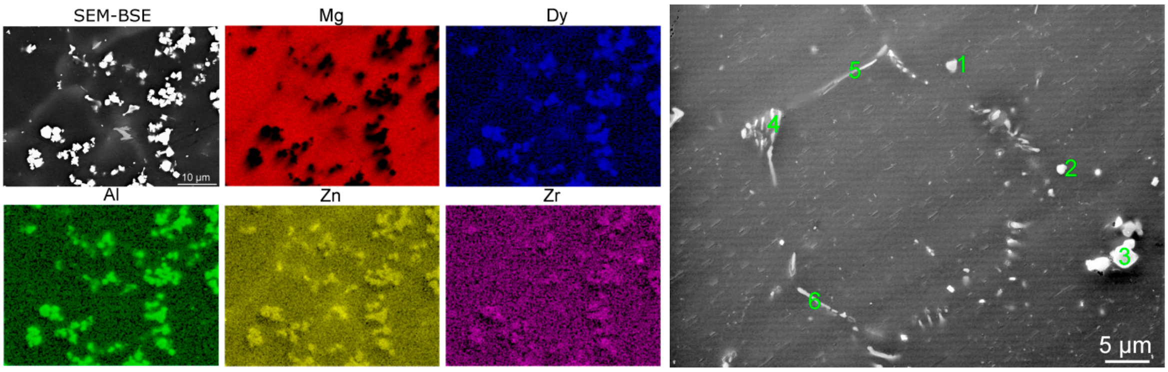

(**a**) (**b**)

Figure 7. (**a**) Distribution of the individual elements within the selected area of the 480 °C/8-h sample; (**b**) detail of the analysed particles in the 480 °C/8-h sample.

Table 3. Chemical compositions of the precipitates in locations 1–3 in Figure 7b (480 °C/8-h sample).

Element (wt. %)	Mg	Al	Zn	Dy	Zr
1	7.51	25.47	0.03	66.97	0.02
2	3.98	31.08	0.04	64.86	0.04
3	3.79	21.33	1.58	73.27	0.03
4	39.46	12.69	8.78	38.98	0.09
5	46.47	9.83	6.66	37.04	0.00
6	32.21	11.02	12.29	44.48	0.00

The variation in the annealing time especially caused variation in the β-phase morphology. The 8 h heat treatment did not provide sufficient energy for the segregated β-phase to dissolve completely. For this reason, the sample still exhibited quite a significant presence of continuous β-phase lamellas along the grain boundaries (Figures 5a and 7a,b). On the other hand, the heat treatment for 16 h provided the material with sufficient energy to dissolve the continuous phase; the elements dissolved into the supersaturated solid solution (SSS) and the β-phase appeared in fine, rather homogeneously distributed elongated particles (not shown here).

3.1.4. Heat Treatment at 560 °C

The SEM-BSE image of the 560 °C/8-h sample structure is depicted in Figure 8. The higher annealing temperature caused significant dissolution of the secondary phases that had formed after casting. According to the EDX analysis, the matrix of both samples contained relatively high amounts of dissolved Dy (4.5 wt. % in average). However, both the heat treated structures still contained secondary phases. Precipitates containing approximately 65 wt. % and 25 wt. % of Dy were those that were mostly present in the 560 °C treated samples. The compositions of a few analysed precipitates depicted in Figure 8b are summarised in Table 4. The annealing time of 8 h turned out to be very favourable; this treatment had the most positive effect on all the structures investigated. The β-phase was present in the discontinuous form of very fine elongated particles and the Dy-rich precipitates were fine and homogeneously distributed. On the other hand, the combination of the high temperature with the annealing time of 16 h resulted in re-precipitation of the β-phase from the SSS in the form of coarse plate-like structures, the detail of which is shown in Figure 8c.

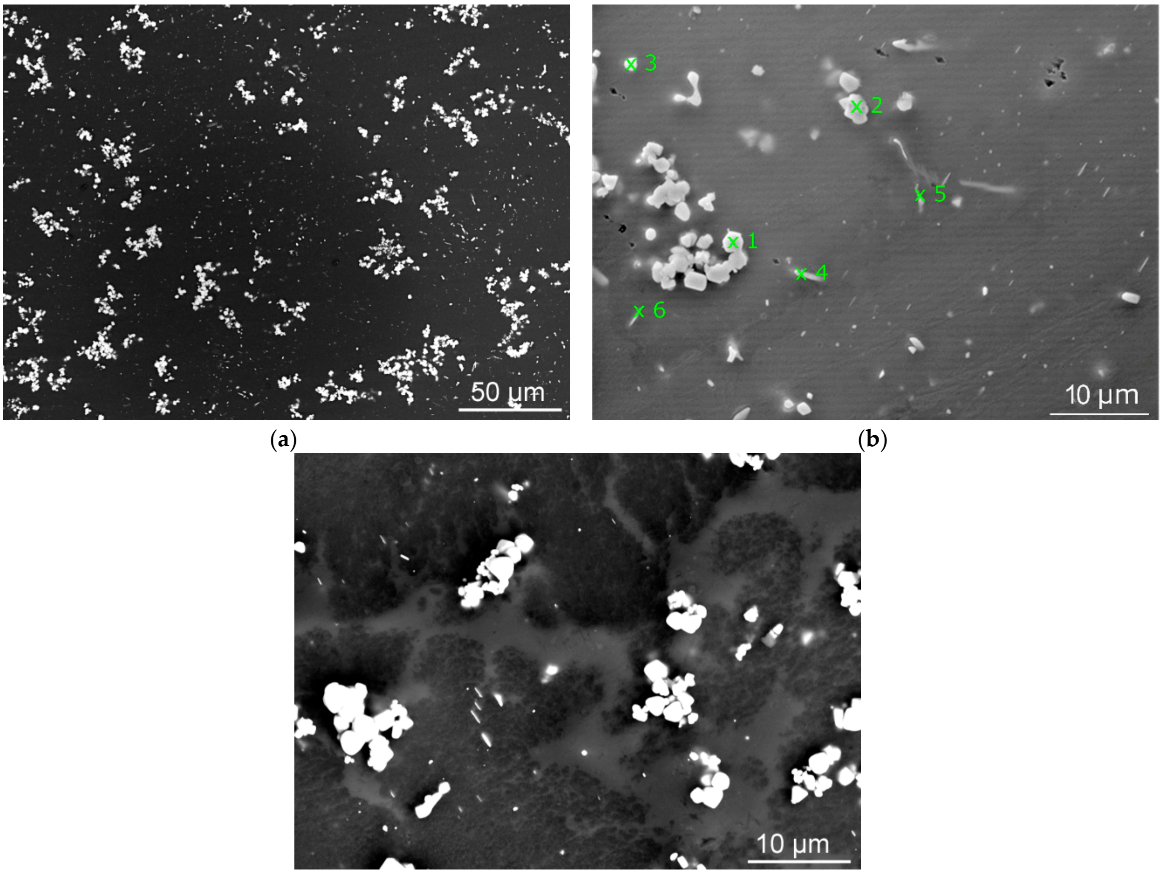

(**a**) (**b**)

(**c**)

Figure 8. SEM-BSE scans of heat treated samples: (**a**) 560 °C/8-h sample; (**b**) analysed locations in the 560 °C/8-h sample; (**c**) detailed image of the secondary phases in the 560 °C/16-h sample.

Table 4. Chemical compositions of the precipitates in locations 1–6 in Figure 8b (560 °C/8-h sample).

Element (wt. %)	Mg	Al	Zn	Dy	Zr
1	2.52	28.30	0.01	69.15	0.03
2	3.38	28.91	0.00	67.69	0.02
3	2.32	27.91	1.08	68.67	0.02
4	49.08	12.69	2.32	35.79	0.12
5	42.61	15.38	2.79	39.22	0.00
6	39.76	14.22	2.33	43.69	0.01

Figure 9a depicts the TEM image of the 560 °C/16-h sample in which three different precipitates were examined. The precipitate in location 1 contained 27 wt. % Mg plus 67 wt. % Dy, 2 wt. % Al and 0.3 wt. % Zn; the precipitate in location 2 consisted of 66.4 wt. % Mg, 24.6 wt. % Dy and 9.0 wt. % Zn; and the precipitate in location 3 contained 60.9 wt. % Mg, 26.8 wt. % Dy and 12.3 wt. % Zn. The distribution maps of the individual elements are shown in Figure 9b. Figure 9c shows the detail of the fine elongated particles (such as particle 3 in Figure 9a) characterised as the 18R-type LPSO phases.

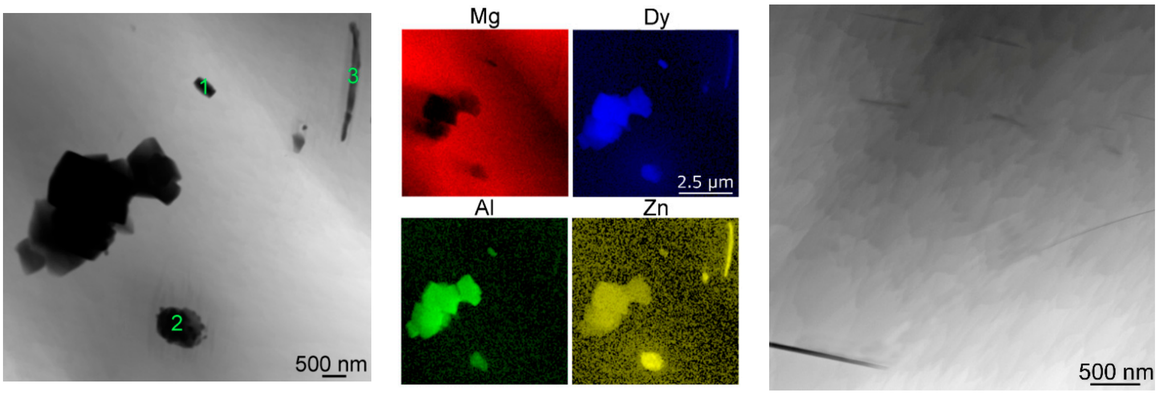

(**a**) (**b**) (**c**)

Figure 9. (**a**) TEM image of precipitates in the 560 °C/16-h sample; (**b**) distributions of the individual elements; (**c**) detail of long-period stacking ordered (LPSO) phases in the 560 °C/16-h sample.

3.2. Characterisation of Precipitates

For each sample, ten images were analysed to calculate the average value. The first analysis dealt with the amount (percentage) of precipitates within the material volume. The analyses were focused on the precipitates that favourably contribute to the mechanical properties. Therefore, only the discrete types of precipitates (polygon-shaped Dy-rich precipitates and discontinuous fine lamellar β-phase particles) were considered; the continuous, coarse and plate-like grain boundary β-phase segregations were neglected. The results are summarised in Table 5 together with the results of the analysis of the average precipitate sizes (the sizes were determined as diameters of circumscribed circles). The results showed the average volume of the fine precipitates to increase with increasing annealing time, except for the 560 °C/16-h sample for which the β-phase re-precipitated at the expense of the other precipitates. However, the precipitates' sizes decreased with increasing annealing time and temperature. Both phenomena are discussed further in Section 4.

Table 5. Characterisation of precipitates after applied heat treatments.

Sample	**480/8**	**480/16**	**520/8**	**520/16**	**560/8**	**560/16**
Avg. volume (%)	4.0	5.8	7.5	8.3	5.8	5.0
Avg. size (μm)	1.93	1.65	1.33	1.25	1.02	0.98

3.3. Microhardness

The results of microhardness measurements in both of the perpendicular directions are summarised in Table 6, in which the average HV (Vickers Hardness) values and the standard deviations are depicted. The lowest microhardness (both the values of approximately 61 HV were more or less comparable) was exhibited by the samples subjected to 480 °C/8 h and 560 °C/16 h heat treatments, while the highest average microhardness value was measured for the samples heat treated at 520 °C, particularly for the 520 °C/8 h sample featuring fine, quite uniformly distributed precipitates. Nevertheless, the differences in the average microhardness being between 61 and 65 HV for all the samples were more or less negligible. On the other hand, deviations from the average values exhibited quite notable differences. Both the samples featuring the lowest microhardness values exhibited the highest deviations of 5 HV from the average values. These phenomena were primarily caused by their inhomogeneous structures. The lowest deviation from the average HV value, only 1.1, was exhibited by the 560 °C/8-h sample; this structure proved to be the most homogeneous from the viewpoint of microhardness. The 520 °C samples also exhibited very uniform microhardness distributions (the deviations from the average values were 1.3 and 1.2 for the 8 h' and 16 h sample, respectively).

Table 6. Average microhardness and standard deviations for all samples.

Sample	480/8	480/16	520/8	520/16	560/8	560/16
Avgerage HV	61.2	62.6	64.6	63.0	61.6	61.9
Standard. deviation	5.2	4.9	1.3	1.2	1.1	4.8

4. Discussion

All of the annealing regimes caused homogenisation of the structure since the as-cast state obviously exhibited significant segregations on the grain boundaries and polygon-shaped precipitates (Figure 1b). The segregations were identified as β-phase of the continuous type, while the polygon-shaped precipitates were rich in Dy and exhibited a mixture of various chemical compositions.

Heat treatment at 480 °C caused partial homogenisation of the structure. Although the temperature was too low for dissolution of the polygon-shaped Dy-rich precipitates (highly stable due to relatively high Dy melting point), the phase segregations along the grain boundaries dissolved the more the longer was the annealing time. The β-phase melting point was reported to be 437 °C [48]. Therefore, at 480 °C, the grain boundary segregations dissolved to the solid solution and re-precipitated in the form of thin elongated β-phase particles, which can for this material be characterised as $Mg_{17}(AlZnDy)_{12}$. This significant change is also advantageous for mechanical properties since grain boundary segregations of brittle $Mg_{17}(Al)_{12}$-type phases have repeatedly been reported to deteriorate strength, as well as the plasticity of Mg-based alloys [19,48,49]. Dy-rich phases usually precipitate from the SSS during ageing—when heat treated at temperatures higher than 300 °C for long time periods (sometimes in hundreds of hours) [32,44]. Nevertheless, increasing the annealing temperature to 480 °C together with decreasing the annealing time to 16 h had similar effects on the precipitation. Therefore, this particular heat treatment not only induced re-formation of strengthening precipitates, but also influenced the β-phase distribution and caused homogenisation of the structure (comparing to conventional ageing treatments at lower temperatures and longer time periods, which usually only have the first mentioned effect). The compositions of the Dy-rich precipitates corresponded to the Mg_3Dy phase, which had been reported to develop in Mg–Dy alloys subjected to annealing temperatures lower than 520 °C [20]. However, the high amount of Al substituting Mg in these precipitates imparts their more precise determination to be $(AlMg)_3Dy$.

The samples treated at 520 °C did not exhibit any notable grain boundary segregation. When compared to 480 °C, the increased temperature caused the alloying elements to dissolve to the SS more intensively, which resulted in the formation of more homogenously distributed fine precipitates, as well as higher amounts of Zn and Dy dissolved in the SS. The dissolubility of Dy in Mg at 520 °C is 22 wt. % [39]. However, rapid solidification introduced by quenching resulted in preserving the non-equilibrium conditions and the formation of phases and compositions slightly different from the assumptions made based on the phase diagrams [50]. Dy was primarily present in the polygon-shaped precipitates with compositions very close to $Mg_{24}(Dy)_5$—i.e., $Mg_{24}(DyZnAl)_5$. According to Rokhlin [20], the ideal temperature for the formation of $Mg_{24}(DyZn)_5$ precipitates is 561 °C. However, some of the particles were identified as a combination of phases, such as $Mg_{24}(DyZnAl)_5$ plus Mg_3Dy. Such combined precipitates occurred in locations with higher concentrations of Dy, which were not able to sufficiently dissolve and homogenise through diffusion due to the relatively low heat treatment temperature and time (found especially in the sample annealed for 8 h). Very fine elongated Dy-rich precipitates, the characterisation of which needed to be performed via TEM, were also found (e.g., location 3 in Figure 4b). These precipitates, identified as the 18R-type LPSO phase, were especially found in the sample annealed for 16 h. The LPSO phases have been reported to develop in Mg–RE (Mg–Zn–RE) alloys subjected to heat treatments at higher temperatures and/or longer times, which provide the alloying elements with sufficient time and energy to perform full diffusion to stacking planes and form these phases [45,51–53]. Although LPSO phases were also observed in the samples annealed at 520 °C (e.g., Table 2), the samples heat treated at 560 °C exhibited their more notable formation (Figure 9c).

The structures annealed at 560 °C featured quite a significant presence of very fine polygon-shaped precipitates and thin elongated precipitates, identified as $Mg_{24}Dy_5$—more precisely $Mg_{24}(DyZn)_5$—phase (containing ~60 wt. % of Dy) and LPSO phases, respectively. Based on the works published by others [20,37], the maximum solubility of Dy in Mg is about 25 wt. % at 561 °C and decreases with decreasing temperature. Therefore, rapid cooling (quenching) from 560 °C resulted in preserving the highest amount of Dy in the matrix of all the investigated annealed samples (approx. 4.5 wt. %). However, the majority of this element was again found in the secondary phases. The 560 °C/16-h sample exhibited significant re-precipitation of the β-phase in the form of coarse plate-like structures (not observed after 8 h annealing), as well as the presence of Dy-rich precipitates and LPSO phases, differing in their morphology although having similar chemical composition—e.g., the morphology of the particles depicted in locations 2 and 3 in Figure 9a pointed to their different nature. The more or less equiaxed-shape precipitate 2 had a cubic lattice corresponding to $(Mg,Zn)_x$ Dy phase [45]. On the other hand, the morphology and composition of the thin elongated precipitate 3 revealed the precipitate to be one of the hexagonal LPSO phases of the 18R type. These phases have been reported to significantly increase mechanical properties by creating obstacles for non-basal slip deformation mechanisms [49].

The average volume of the fine precipitates in the 480 °C/8-h sample was 4%. This corresponds to the fact that most of the alloying elements were still conserved in the grain boundary segregations formed during casting and did not have sufficient energy to re-precipitate. On the other hand, the longer annealing time of 16 h caused the volume of precipitates to increase to 5.8%. This was mostly due to the better dissolution of the continuous β-phase. The average precipitate size for this annealing temperature was the highest of all those investigated due to the insufficient dissolution and aggravated diffusion. The precipitates were mostly fragments of those that had formed during casting and subsequent quenching. The activation energy was insufficient for the diffusion to proceed effectively.

The samples that were annealed at 520 °C exhibited an increase in the presence of precipitates; however, their average size decreased slightly. The higher annealing temperature provided sufficient energy for the β-phase to dissolve and supported the diffusion process. The polygon-shaped precipitates re-precipitated as well and their chemical composition changed slightly when compared to the 480 °C samples. Nevertheless, the temperature and time were still not sufficient for the elements to dissolve into the SS to a greater extent and subsequent quenching caused precipitation of various phases from the SSS. On the other hand, most of the coarse precipitates formed during cooling after casting dissolved and subsequently the formation of new fine precipitates from the SSS occurred during quenching. For this reason, the precipitates refined and their average size was smaller than for the 480 °C treated samples.

Samples annealed at 560 °C exhibited a decrease in the presence and size of precipitates; Dy was dissolved in the solid solution in the greatest extent. The volume of precipitates in the 560 °C/8-h sample was slightly higher than in the 560 °C/16-h sample (5.8% compared to 5%); however, the 16 h' sample exhibited re-precipitation of the continuous β-phase, which was neglected during these analyses. The average precipitate size in both the samples was approximately 1 µm, which was the smallest of all the investigated states. This was caused by the annealing temperature, which provided all the alloying elements with favourable solubility, as well as simplified diffusion. These phenomena finally contributed to the formation of very fine precipitates during subsequent quenching.

As reported by Rokhlin [20], (micro)hardness measurement is an advantageous method to evaluate structural changes in Mg–RE alloys. For all the samples, the differences between both the measured diagonals were negligible. However, all of the samples exhibited variations along the measured directions. The 480 °C/8-h sample exhibited the largest variation in HV values along the measured diagonals. This phenomenon was caused by the inhomogeneous precipitate distribution and their occurrence in clusters (as already mentioned, the observed precipitates were mostly fragments of the larger particles developed after casting, a significant portion of the alloying elements was still conserved in the β-phase at the original grain boundaries); the large precipitates mostly cracked when loaded by the indenter and caused local brittleness. The average microhardness increased slightly for the sample annealed for 16 h, in which the hard and brittle β-phase dissolved significantly. However, the precipitates were still too large to contribute substantially to the mechanical properties (similar effect as over-ageing [20]). The 520 °C samples exhibited more uniform HV0.2 distribution due to the more or less homogeneous distribution of finer precipitates. Precipitation of the alloying elements in fine Dy-rich polygon-shaped and the β-phase fine elongated particles increased the microhardness similarly as optimised ageing treatment [41]. However, the sample that was annealed for 16 h exhibited a slight decrease in HV values. The increased annealing time resulted in the dissolution of a portion of the alloying elements into the SS, which decreased microhardness, but would most probably slightly increase the strength and improve the plastic properties. An increase in the annealing temperature to 560 °C caused a slight decrease in the microhardness for the 8-h sample—due to further dissolution of the alloying elements—and an increase for the 16-h sample. This ensues from the nature of the structures. While the 560 °C/8-h sample exhibited fine and quite homogeneously distributed precipitates, the 16-h sample featured plate-like β-phase precipitates that were very hard but also very brittle [52].

Based on the results, the 560 °C/8-h heat treatment regime would most probably impart the most advantageous mechanical properties (strength, as well as plasticity) due to the favourable size and homogeneous distribution of precipitates, as well as the presence of fine LPSO phases. A deeper study of the mechanical properties imparted by this heat treatment regime and the precipitation kinetics is planned for a consequent publication.

5. Conclusions

All of the investigated material states featured a solid solution (Mg-based matrix) and several types of secondary phases rich in the alloying elements. However, the solid solution in all the samples also contained dissolved Al, Zn and Dy, the amounts of which depended primarily on the heat treatment temperature. All of the samples exhibited the presence of β-phase and polygon-shaped Dy-rich precipitates. The heat treatment temperature of 480 °C was not sufficient for the structure to homogenise, and especially the sample annealed for 8 h exhibited β-phase grain boundary segregations that dissolved more with a higher annealing temperature and time. However, annealing at 560 °C for 16 h caused re-precipitation of the β-phase in the form of coarse plates. Dy-rich precipitates decreased their size and increased the uniformity of their distribution with increasing annealing temperature and time within the whole range of investigated regimes. The microhardness ranged between 60 and 65 HV; the differences between the samples were thus not remarkable. However, their uniformity (variations in the average value) varied significantly. The most uniform were the values for the samples heat treated at 520 °C/16 h and 560 °C/8 h. The latter was the most favourable from the conjunct viewpoints of structure homogeneity, size of precipitates and microhardness distribution.

Acknowledgments: This paper was created in the Project No. LO1203 "Regional Materials Science and Technology Centre—Feasibility Program" funded by the Ministry of Education, Youth and Sports of the Czech Republic.

Author Contributions: Radim Kocich and Lenka Kunčická both cooperated on designing the experiment as well as writing the article. Radim Kocich then primarily conducted the experimental work concerning heat treating the samples, while Lenka Kunčická primarily performed and evaluated the microscopic analyses.

Conflicts of Interest: The authors declare no conflict of interest. The founding sponsors had no role in the design of the study, in the collection, analyses, or interpretation of data, in the writing of the manuscript, or in the decision to publish the results.

References

1. Joost, W.J.; Krajewski, P.E. Towards magnesium alloys for high-volume automotive applications. *Scr. Mater.* **2017**, *128*, 107–112. [CrossRef]

2. Mouritz, A.P. Magnesium alloys for aerospace structures. In *Introduction to Aerospace Materials*; Woodhead Publishing: Cambridge, UK, 2012; pp. 224–231, ISBN 1855739461. [CrossRef]
3. Radha, R.; Sreekanth, D. Insight of magnesium alloys and composites for orthopedic implant applications—A review. *J. Magnes. Alloys* **2017**, *3*, 286–312. [CrossRef]
4. Kuncicka, L.; Kocich, R.; Lowe, T.C. Advances in metals and alloys for joint replacement. *Prog. Mater. Sci.* **2017**, *88*, 232–280. [CrossRef]
5. Wang, L.; Qiao, Q.; Liu, Y.; Song, X. Formability of AZ31 Mg alloy sheets within medium temperatures. *J. Magnes. Alloys* **2013**, *1*, 312–317. [CrossRef]
6. Du, J.; Yang, J.; Kuwabara, M.; Li, W.; Peng, J. Effect of strontium on the grain refining efficiency of Mg-3Al alloy refined by carbon inoculation. *J. Alloys Compd.* **2009**, *470*, 228–232. [CrossRef]
7. Lukac, P.; Kocich, R.; Greger, M.; Padalka, O.; Szaraz, Z. Microstructure of AZ31 and AZ61 Mg alloys prepared by rolling and ECAP. *Kov. Mater. Mater.* **2007**, *45*, 115–120.
8. Kocich, R.; Kunčická, L.; Macháčková, A. Twist Channel Multi-Angular Pressing (TCMAP) as a method for increasing the efficiency of SPD. In *IOP Conference Series: Materials Science and Engineering*; IOP Publishing Ltd.: Bristol, UK, 2014; Volume 63, p. 12006. [CrossRef]
9. Kocich, R.; Kursa, M.; Macháčková, A. FEA of Plastic Flow in AZ63 Alloy during ECAP Process. *Acta Phys. Pol. A* **2012**, *122*, 581–587. [CrossRef]
10. Kunčická, L.; Kocich, R.; Drápala, J.; Andreyachshenko, V.A. FEM simulations and comparison of the ECAP and ECAP-PBP influence on Ti6Al4V alloy's deformation behaviour. In Proceedings of the METAL 2013, 22nd International Conference on Metallurgy and Materials, Brno, Czech Republic, 15–17 May 2013; Tanger Ltd.: Ostrava, Czech Republic, 2013; pp. 391–396.
11. Kunčická, L.; Lowe, T.C.; Davis, C.F.; Kocich, R.; Pohludka, M. Synthesis of an Al/Al_2O_3 composite by severe plastic deformation. *Mater. Sci. Eng. A* **2015**, *646*, 234–241. [CrossRef]
12. Greger, M.; Kocich, R. Superplasticity of magnesium alloys. In Proceedings of the METAL 2011, 20th Anniversary International Conference on Metallurgy and Materials, Brno, Czech Republic, 18–20 May 2011; Tanger Ltd.: Ostrava, Czech Republic, 2011; pp. 421–424.
13. Hou, L.; Li, B.; Wu, R.; Cui, L.; Ji, P.; Long, R.; Zhang, J.; Li, X.; Dong, A.; Sun, B. Microstructure and mechanical properties at elevated temperature of Mg-Al-Ni alloys prepared through powder metallurgy. *J. Mater. Sci. Technol.* **2017**, *33*, 947–953. [CrossRef]
14. Kocich, R.; Kunčická, L.; Dohnalík, D.; Macháčková, A.; Šofer, M. Cold rotary swaging of a tungsten heavy alloy: Numerical and experimental investigations. *Int. J. Refract. Met. Hard Mater.* **2016**, *61*, 264–272. [CrossRef]
15. Peng, Q.; Wang, L.L.; Wu, Y. Structure stability and strengthening mechanism of die-cast Mg-Gd-Dy based alloy. *J. Alloys Compd.* **2009**, *469*, 587–592. [CrossRef]
16. Zhang, Z.; Liu, X.; Wang, Z.; Le, Q.; Hu, W.; Bao, L.; Cui, J. Effects of phase composition and content on the microstructures and mechanical properties of high strength Mg–Y–Zn–Zr alloys. *Mater. Des.* **2015**, *88*, 915–923. [CrossRef]
17. Shi, F.; Wang, C.; Zhang, Z. Microstructures, corrosion and mechanical properties of as-cast Mg–Zn–Y–(Gd) alloys. *Trans. Nonferrous Met. Soc. China* **2015**, *25*, 2172–2180. [CrossRef]
18. Russell, A.; Lee, K.L. *Structure-Property Relations in Nonferrous Metals*, 1st ed.; John Wiley & Sons, Inc.: Hoboken, NJ, USA, 2005; ISBN 978-0-471-64952-6.
19. Kocich, R.; Greger, M.; Macháčková, A.; Bořuta, J. Investigation of plasticity in Mg-Zn-Al based magnesium alloys with graded aluminium content. In Proceedings of the METAL 2009, 18th International Conference on Metallurgy and Materials, Hradec nad Moravicí, Czech Republic, 19–21 May 2009; Tanger Ltd.: Ostrava, Czech Republic, 2009; pp. 525–531.
20. Rokhlin, L.L. *Advances in Metallic Alloys Volume 3—Magnesium Alloys Containing Rare Earth Metals: Structure and Properties*, 1st ed.; Taylor and Francis: New York, NY, USA, 2003; ISBN 978-0415284141.
21. Singh, A.; Osawa, Y.; Somekawa, H.; Mukai, T. Ultra-fine grain size and isotropic very high strength by direct extrusion of chill-cast Mg–Zn–Y alloys containing quasicrystal phase. *Scr. Mater.* **2011**, *64*, 661–664. [CrossRef]
22. Ayman, E.; Junko, U.; Katsuyoshi, K. Application of rapid solidification powder metallurgy to the fabrication of high-strength, high-ductility Mg–Al–Zn–Ca–La alloy through hot extrusion. *Acta Mater.* **2011**, *59*, 273–282. [CrossRef]

23. Zhang, J.; Leng, Z.; Liu, S.; Li, J.; Zhang, M.; Wu, R. Microstructure and mechanical properties of Mg-Gd-Dy-Zn alloy with long period stacking ordered structure or stacking faults. *J. Alloys Compd.* **2011**, *509*, 7717–7722. [CrossRef]
24. Yang, X.; Wu, S.; Lü, S.; Hao, L.; Fang, X. Refinement of LPSO structure in Mg-Ni-Y alloys by ultrasonic treatment. *Ultrason. Sonochem.* **2018**, *40*, 472–479. [CrossRef] [PubMed]
25. Gu, X.N.; Li, N.; Zheng, Y.F.; Ruan, L. In vitro degradation performance and biological response of a Mg–Zn–Zr alloy. *Mater. Sci. Eng. B* **2011**, *176*, 1778–1784. [CrossRef]
26. Zhang, J.; Xin, C.; Cheng, W.; Bian, L.; Wang, H.; Xu, C. Research on long-period-stacking-ordered phase in Mg–Zn–Dy–Zr alloy. *J. Alloys Compd.* **2013**, *558*, 195–202. [CrossRef]
27. King, J.F. Development of Practical high Temperature Magnesium Casting Alloys. In *Magnesium Alloys and Their Application*; Kainer, K.U., Ed.; Wiley-VCH: Weinheim, Germany, 2000; pp. 14–22, ISBN 9783527302826.
28. Khosroshahi, A.R. The microstructure and creep of an extruded Mg–Y–Nd alloy. In *Magnesium Alloys and Their Application*; Kainer, K.U., Ed.; Wiley-VCH: Weinheim, Germany, 2000; pp. 711–715, ISBN 9783527302826.
29. Herchenroeder, J.; Manfrinetti, P.; Gschneidner, K. Physical metallurgy of metassbcc lanthanide-magnesium alloys for R = La, Gd, and Dy. *Metall. Mater. Trans. A* **1989**, *20*, 1575–1583. [CrossRef]
30. Meng, F.; Rosalie, J.M.; Singh, A.; Somekawa, H.; Tsuchiya, K. Ultrafine grain formation in Mg–Zn alloy by in situ precipitation during high-pressure torsion. *Scr. Mater.* **2014**, *78–79*, 57–60. [CrossRef]
31. Rosalie, J.M.; Somekawa, H.; Singh, A.; Mukai, T. The effect of size and distribution of rod-shaped β1 precipitates on the strength and ductility of a Mg–Zn alloy. *Mater. Sci. Eng. A* **2012**, *539*, 230–237. [CrossRef]
32. Li, D.; Dong, J.; Zeng, X.; Lu, C.; Ding, W. Characterization of precipitate phases in a Mg–Dy–Gd–Nd alloy. *J. Alloys Compd.* **2007**, *439*, 254–257. [CrossRef]
33. Kim, W.J.; Park, I.B.; Han, S.H. Formation of a nanocomposite-like microstructure in Mg–6Al–1Zn alloy. *Scr. Mater.* **2012**, *66*, 590–593. [CrossRef]
34. Alaneme, K.K.; Okotete, E.A. Enhancing plastic deformability of Mg and its alloys—A review of traditional and nascent developments. *J. Magnes. Alloys* **2017**. [CrossRef]
35. Gu, X.N.; Li, N.; Zheng, Y.F.; Kang, F.; Wang, J.T.; Ruan, L. In vitro study on equal channel angular pressing AZ31 magnesium alloy with and without back pressure. *Mater. Sci. Eng. B* **2011**, *176*, 1802–1806. [CrossRef]
36. Yang, L.; Huang, Y.; Feyerabend, F.; Willumeit, R.; Kainer, K.U.; Hort, N. Influence of ageing treatment on microstructure, mechanical and bio-corrosion properties of Mg–Dy alloys. *J. Mech. Behav. Biomed. Mater.* **2012**, *13*, 36–44. [CrossRef] [PubMed]
37. Yang, L.; Huang, Y.; Peng, Q.; Feyerabend, F.; Kainer, K.U.; Willumeit, R.; Hort, N. Mechanical and corrosion properties of binary Mg–Dy alloys for medical applications. *Mater. Sci. Eng. B* **2011**, *176*, 1827–1834. [CrossRef]
38. Biesiekierski, A.; Wang, J.; Gepreel, M.A.-H.; Wen, C. A new look at biomedical Ti-based shape memory alloys. *Acta Biomater.* **2012**, *8*, 1661–1669. [CrossRef] [PubMed]
39. Yang, L.; Huang, Y.; Feyerabend, F.; Willumeit, R.; Mendis, C.; Kainer, K.U.; Hort, N. Microstructure, mechanical and corrosion properties of Mg–Dy–Gd–Zr alloys for medical applications. *Acta Biomater.* **2013**, *9*, 8499–8508. [CrossRef] [PubMed]
40. Choudhary, L.; Singh Raman, R.K. Mechanical integrity of magnesium alloys in a physiological environment: Slow strain rate testing based study. *Eng. Fract. Mech.* **2013**, *103*, 94–102. [CrossRef]
41. Kocich, R.; Kunčická, L.; Král, P.; Lowe, T.C. Texture, deformation twinning and hardening in a newly developed Mg–Dy–Al–Zn–Zr alloy processed with high pressure torsion. *Mater. Des.* **2016**, *90*, 1092–1099. [CrossRef]
42. Li, J.; He, Z.; Fu, P.; Wu, Y.; Peng, L.; Ding, W. Heat treatment and mechanical properties of a high-strength cast Mg–Gd–Zn alloy. *Mater. Sci. Eng. A* **2016**, *651*, 745–752. [CrossRef]
43. Zheng, J.; Chen, B. Interactions between long-period stacking ordered phase and β′ precipitate in Mg–Gd–Y–Zn–Zr alloy: Atomic-scale insights from HAADF-STEM. *Mater. Lett.* **2016**, *176*, 223–227. [CrossRef]
44. Apps, P.J.; Karimzadeh, H.; King, J.F.; Lorimer, G.W. Precipitation reactions in magnesium-rare earth alloys containing yttrium, gadolinium or dysprosium. *Scr. Mater.* **2003**, *48*, 1023–1028. [CrossRef]
45. Stulikova, I.; Smola, B. Mechanical properties and phase composition of potential biodegradable Mg–Zn–Mn-base alloys with addition of rare earth elements. *Mater. Charact.* **2010**, *61*, 952–958. [CrossRef]

46. Bi, G.; Fang, D.; Zhao, L.; Lian, J.; Jiang, Q.; Jiang, Z. An elevated temperature Mg–Dy–Zn alloy with long period stacking ordered phase by extrusion. *Mater. Sci. Eng. A* **2011**, *528*, 3609–3614. [CrossRef]
47. Bi, G.; Li, Y.; Huang, X.; Chen, T.; Ma, Y.; Hao, Y. Deformation behavior of an extruded Mg-Dy-Zn alloy with long period stacking ordered phase. *J. Magnes. Alloys* **2015**, *3*, 63–69. [CrossRef]
48. Ravi Kumar, N.V.; Blandin, J.J.; Suéry, M. Effect of Thermomechanical Treatments on the Microstructure of AZ91 Alloy. In *Magnesium Alloys and Their Application*; Kainer, K.U., Ed.; Wiley-VCH: Weinheim, Germany, 2000; pp. 161–167, ISBN 9783527302826.
49. Braszczyńska-Malik, K. Precipitates of Gamma-Mg17Al12 Phase in AZ91 Alloy. In *Magnesium Alloys—Design, Processing and Properties*; Czerwinski, F., Ed.; InTech: London, UK, 2011; pp. 95–112. [CrossRef]
50. Calculated Dy–Mg Phase Diagram. Available online: http://resource.npl.co.uk/mtdata/phdiagrams/dymg.htm (accessed on 15 December 2017).
51. Luo, X.M.; Bi, G.L.; Jiang, J.; Li, M.; Li, R.G.; Li, Y.D.; Ma, Y.; Hao, Y. Compressive anisotropy of extruded Mg–Dy–Zn alloy sheet. *Trans. Nonferrous Met. Soc. China* **2016**, *26*, 390–397. [CrossRef]
52. Wu, Y.J.; Xu, C.; Zheng, F.Y.; Peng, L.M.; Zhang, Y.; Ding, W.J. Formation and characterization of microstructure of as-cast Mg–6Gd–4Y–xZn–0.5Zr (x = 0.3, 0.5 and 0.7 wt.%) alloys. *Mater. Charact.* **2013**, *79*, 93–99. [CrossRef]
53. Zhao, X.; Shi, L.; Xu, J. Biodegradable Mg–Zn–Y alloys with long-period stacking ordered structure: Optimization for mechanical properties. *J. Mech. Behav. Biomed. Mater.* **2013**, *18*, 181–190. [CrossRef] [PubMed]